

# Distortion matrix concept for deep imaging in optical coherence microscopy

Amaury Badon<sup>1</sup>, Victor Barolle<sup>1</sup>, Kristina Irsch<sup>2</sup>, Albert C. Boccara<sup>1</sup>,  
Mathias Fink<sup>1</sup>, and Alexandre Aubry<sup>1,\*</sup>

<sup>1</sup> Institut Langevin, ESPCI Paris, CNRS, PSL University, 1 rue Jussieu, 75005 Paris, France

<sup>2</sup>Institut de la Vision, CIC 1423, UPMC-Sorbonne Universities  
UMR 968, INSERM U968, CNRS UMR 7210, Quinze-Vingts National Eye Hospital, France

\*To whom correspondence should be addressed; E-mail: alexandre.aubry@espci.fr.

**In optical imaging, light propagation is affected by the inhomogeneities of the medium. Sample-induced aberrations and multiple scattering can strongly degrade the image resolution and contrast. Based on a dynamic correction of the incident and/or reflected wave-fronts, adaptive optics has been employed to compensate for those aberrations. However, it mainly applies to spatially-invariant aberrations or to thin aberrating layers. Here, we propose a global and non-invasive approach based on the distortion matrix concept. This matrix basically connects any focusing point of the image with the distorted part of its wave-front in reflection. A time-reversal and entropy analysis of the distortion matrix allows to correct for high-order aberrations and forward multiple scattering over multiple isoplanatic areas. Proof-of-concept experiments are performed through biological tissues and an opaque cornea. We demonstrate a Strehl ratio enhancement up to 2500 and recover a diffraction-limited resolution until a depth of ten scattering mean free paths.**

# INTRODUCTION

For decades, optical microscopy has been a vital tool in biomedical research to observe live specimen with a sub-micron resolution and with minimum invasiveness. Yet, imaging conditions required for such exquisite performances are rarely gathered. For instance, both the resolution and the contrast drop as the imaging depth increases inside a biological tissue. This observation is a consequence of the spatial variations of the specimen refractive index that distort the wave-front of both the incoming and outgoing light. When these variations exhibits low spatial frequencies we use the term aberrations while scattering describes the effect of the higher spatial variations. Both these effects limit the use of conventional microscopy to shallow depths or to semi-transparent specimens. Imaging deeper requires to simultaneously compensate for these detrimental phenomena.

To mitigate the aberrations induced by the specimen, the concept of adaptive optics (AO) has been adapted to microscopy from astronomy where it was developed decades ago (*1, 2*). Indeed, astronomers faced the same impediment as fluctuations in the atmosphere severely distort the wave-front of the light coming from stars and prevent to obtain a diffraction-limited stellar image. Astronomers then proposed to measure these distortions using a wave-front sensor and to counterbalance it with a dynamic programmable element such as deformable mirrors. Following this concept and the development of deformable mirrors with increasing number of elements, AO already demonstrated its benefits in various imaging techniques such as digital holography (*3, 4*), confocal microscopy (*5, 6*), two-photon microscopy (*7–9*), or optical coherence tomography (OCT) (*10, 11*). Unfortunately, AO methods usually require a guide star and are limited to a small region called the isoplanatic patch (IP), the area over which the aberrations can be considered as spatially-invariant. Therefore, there is a need to extend the field-of-view (FOV) of AO methods by tackling the case of multiple IPs. This issue is particularly decisive

for deep imaging where IP size becomes extremely tiny:  $<10\ \mu\text{m}$  beyond a depth of 1 mm (12).

On the other hand, multiple scattering was long thought to be too complex to be compensated. For deep imaging, a gating mechanism is generally used to reject the multiply-scattered photons and capture only the ballistic light. This gating can be spatial (13) as in confocal microscopy or temporal (14) as in optical coherence tomography, but they are still depth limited as they rely on the exponentially attenuated ballistic light. In a pioneering experiment, Vellekoop and Mosk demonstrated in 2007 the possibility to restore a diffraction-limited spot through a scattering medium by properly shaping the incoming light (15). Subsequently, a matrix approach to light propagation through complex media was developed (16). Relying on the measurement of the Green's functions between each pixel of a spatial light modulator (SLM) and of a charge-coupled device (CCD) camera across a scattering medium, the experimental access to the transmission matrix allows taking advantage of MS for optimal light focusing (16) and communication across a diffusive layer (17, 18) or a multimode fiber (19, 20). However, a transmission configuration is not adapted to non-invasive and/or in-vivo imaging of biological media. An epi-detection geometry should thus be considered. During the last few years, the reflection matrix  $\mathbf{R}$  had been investigated to perform selective focusing/detection in multi-target media (21, 22) and energy delivery (23, 24) through strongly scattering media. With regards to the specific purpose of imaging, the matrix approach has been recently used to implement AO tools in post-processing. The single scattering component of the reflected wave-field through biological tissues has been enhanced in depth by compensating for high-order aberrations (25, 26).

In this paper, we propose to go beyond a matrix approach of AO by introducing a novel operator: the so-called distortion matrix  $\mathbf{D}$ . Unlike previous works that investigated  $\mathbf{R}$  either in the focal plane (22) or the pupil plane (21, 25, 26), we here consider the medium response between those dual bases (27, 28). Unlike  $\mathbf{R}$ , the  $\mathbf{D}$ -matrix does not consider the reflected wave-field as a building block but its deviation from an ideal wave-front that would be obtained

in absence of aberrations and without multiple scattering. This operation may seem trivial but dramatically highlights the input/output correlations of the wave-field. While the canonical reflection matrix exhibits a random feature in a turbid medium, the distortion matrix displays strong field-field correlations over each IP. Thanks to this new operator, some relevant results of information theory can thus be fruitfully applied to optical imaging. A time-reversal analysis of  $\mathbf{D}$  allows to decompose the FOV into several isoplanatic modes. Mathematically, it consists in a singular value decomposition (SVD) of  $\mathbf{D}$  that maps each isoplanatic mode onto the associated wave-front distortion in the pupil plane. The Shannon entropy  $\mathcal{H}$  of the singular values allows to define the effective rank of the imaging problem. A combination of the  $\mathcal{H}$  first eigenstates yields an image of the focal plane with an excellent contrast and a diffraction-limited resolution as if the medium ahead was made perfectly transparent.

Several experiments with an increasing order of complexity are presented to demonstrate the benefits of the  $\mathbf{D}$ -matrix for optical imaging in turbid media. For sake of simplicity, the first experiment involves the imaging of a single IP through a thick layer of biological tissues. This configuration allows to lay down the  $\mathbf{D}$ -matrix concept and highlight the physics behind it. Then, a second proof-of-concept experiment considers a thin but strong aberrating layer introduced between the microscope objective and a resolution target. This imaging configuration involves a spatially-varying aberration across the FOV (*i.e* several IPs). At last, we describe an imaging experiment through an opaque non-human primate cornea that induces high-order aberrations (including forward multiple scattering) and a strong diffuse multiple scattering background. The  $\mathbf{D}$ -matrix decomposes the imaging problem into a set of IP modes whose degree of complexity increases with their rank (*i.e* smaller spatial extent in the focal plane and higher phase distortion in the pupil plane). This last experiment demonstrates the ability of our matrix approach to discriminate between forward multiple scattering paths that can be taken advantage of for imaging and the diffuse background that shall be removed from the final image.



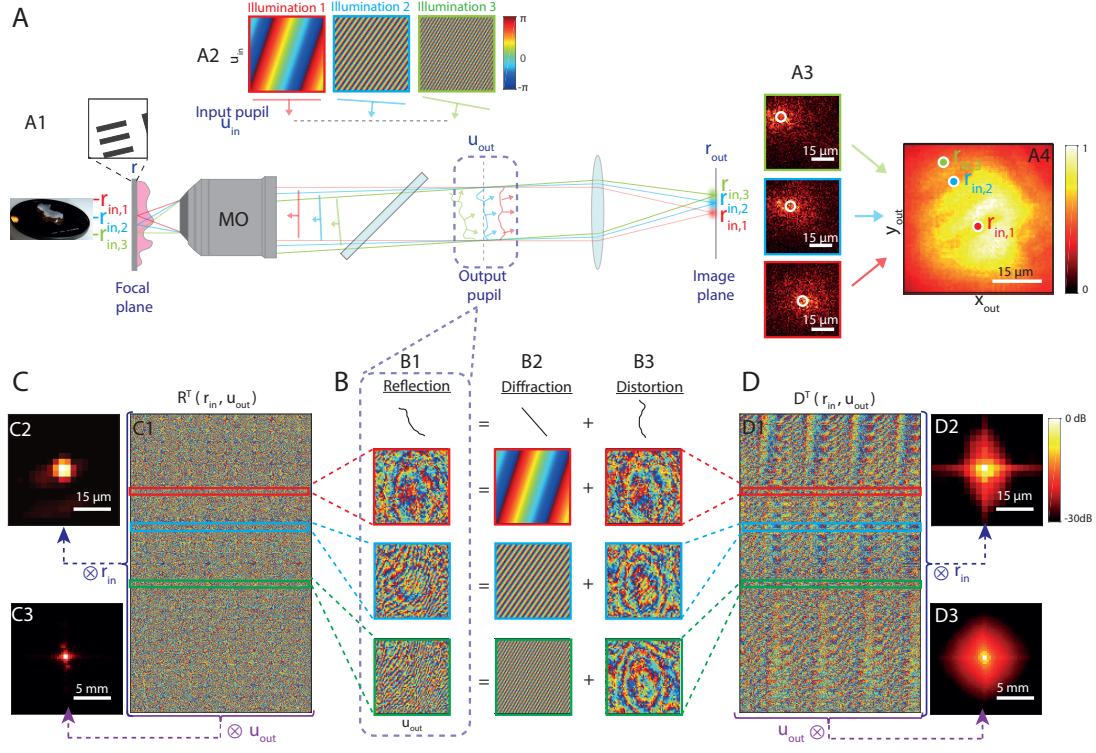


**Figure 1: Principle of the distortion matrix approach.** (A) A resolution target (USAF 1951) is positioned underneath a 800- $\mu\text{m}$ -thick rat intestine sample (A1). In scanning microscopy, raster scanning in the focal plane is obtained using a set of successive plane wave illuminations in the input pupil (A2). In presence of aberrations between the MO and the object, the detected intensity will exhibit a much larger extent compared to the ideal point spread function (A3). The resulting full-field image displays a low contrast and a reduced resolution (A4). (B), In the output pupil plane, the phase of the reflected wave-fields (B1) can be split into a diffraction (B2) and a distortion (B3) term. (C) The reflected wave-fields can be stored along column vectors and form the reflection matrix  $\mathbf{R} = [R(\mathbf{u}_{\text{out}}, \mathbf{r}_{\text{in}})]$ . The phase of  $\mathbf{R}^\top$  is displayed in (C1). The auto-correlations of the reflected wave-fields are computed in the focal (C2) and in the pupil (C3) planes, both in dB. (D) The distorted wave-fields can be stored along column vectors and form the distortion matrix  $\mathbf{D} = [D(\mathbf{u}_{\text{out}}, \mathbf{r}_{\text{in}})]$ . The phase of  $\mathbf{D}^\top$  is displayed in (D1). The auto-correlations of the distorted wave-fields are displayed in the focal (D2) and pupil (D3) planes, both in dB. All the data shown here are extracted from the rat intestine imaging experiment.

# RESULTS

## Time-gated reflection matrix

The  $\mathbf{D}$ -matrix concept first relies on the measurement of the time-gated reflection matrix  $\mathbf{R}$  from the scattering sample. Until now, optical transmission/reflection matrices have always been investigated either in the  $\mathbf{k}$  space (plane-wave basis) (16, 25) or in the real space (22). Here the  $\mathbf{R}$ -matrix will be defined between those dual bases. The experimental set-up has already been described in a previous work (22) and is displayed in Fig. S1. The experimental procedure is detailed in the Methods section. The sample is illuminated through a microscope objective (MO) by a set of focused waves (input focusing basis) (see Fig. 1A). For each illumination, the amplitude and phase of the reflected wave-field is recorded by phase-shifting interferometry on a CCD camera placed in the pupil plane (output pupil basis, see Fig. 1B1). A coherent time gating is also applied in order to select ballistic and snake photons while eliminating a (large) part of the diffuse photons (see Fig. S1). A set of time gated reflection coefficients,  $R(\mathbf{u}_{\text{out}}, \mathbf{r}_{\text{in}})$ , is finally measured between each virtual source in the focal plane identified by the vectors  $\mathbf{r}_{\text{in}}$  at the input and each point of the pupil plane  $\mathbf{u}_{\text{out}}$  at the output. These coefficients form the reflection matrix  $\mathbf{R}$  (see Fig. 1C1).

The first imaging problem we consider in this paper deals with an experiment through biological tissues (see Fig. 1A). A positive U.S. Air Force (USAF) 1951 resolution target placed behind an 800- $\mu\text{m}$ -thick layer of rat intestine tissues is imaged through an immersion objective [40 $\times$ , NA (numerical aperture), 0.8; Olympus]. The rat intestine tissues display a refractive index  $n \sim 1.4$ , a scattering mean free path  $\ell_s$  of the order of 100  $\mu\text{m}$  and an anisotropy factor  $g \simeq 0.9$  (29). This experimental configuration corresponds to an imaging condition for which time gating guarantees that the reflection matrix mostly contains ballistic or snake photons reflected by the resolution target (30). The reflection matrix  $\mathbf{R}$  is measured over a FOV

$F = 41 \times 41 \mu\text{m}^2$  with  $N_{in} = 729$  input wave-fronts, a spatial sampling  $\delta r_{in} = 1.6 \mu\text{m}$  and an input pupil aperture  $\mathcal{D}_{in} = 1.7 \times 1.7 \text{ mm}^2$ . At the output, the wave-field is recorded over a pupil size of  $\mathcal{D}_{out} = 4.5 \times 4.5 \text{ mm}^2$  with  $N_{out} = 6084$  pixels and a spatial sampling  $\delta u_{out} = 58 \mu\text{m}$ .

Figure 1B1 displays examples of reflected wave-fields for several virtual sources  $\mathbf{r}_{in}$ . Each wave-field is stored along a column vector and forms the reflection matrix  $\mathbf{R} = [R(\mathbf{u}_{out}, \mathbf{r}_{in})]$  (Fig. 1C1).  $\mathbf{R}$  exhibits a 4D-structure but is concatenated both at input and output to be displayed in 2D (see Fig. S2). The phase of  $\mathbf{R}$  is displayed in Fig. 1C1. Its spatial and angular correlations in the focal and pupil planes are displayed in Figs. 1C2 and C3, respectively. As it could be conjectured from the column vectors displayed in Fig. 1B1, the matrix  $\mathbf{R}$  only displays short-range correlations. This is quite surprising as the object to be imaged is deterministic and contained in a single IP.

## Principle of the distortion matrix

To understand this seemingly randomness of  $\mathbf{R}$  and reveal its hidden correlations, we now investigate its theoretical expression. The reflection matrix can be expressed as follows (see Fig. S3):

$$\mathbf{R} = \mathbf{G}\mathbf{\Gamma}\mathbf{H}_{in} \quad (1)$$

or, in terms of matrix coefficients,

$$R(\mathbf{u}_{out}, \mathbf{r}_{in}) = \int_F d\mathbf{r} G(\mathbf{u}_{out}, \mathbf{r}) \underbrace{\gamma(\mathbf{r}) H_{in}(\mathbf{r}, \mathbf{r}_{in})}_{S(\mathbf{r}, \mathbf{r}_{in})} \quad (2)$$

$\mathbf{H}_{in} = [H_{in}(\mathbf{r}, \mathbf{r}_{in})]$  is the input focusing matrix. Its columns are none other than the input focal spots centered around each focusing point  $\mathbf{r}_{in}$  (see Fig. S3). Under a single scattering assumption,  $\mathbf{\Gamma}$  is a diagonal matrix whose elements  $\gamma(\mathbf{r})$  are the reflectivity of the scattering medium in the focal plane. The illumination/reflectivity product  $S(\mathbf{r}, \mathbf{r}_{in}) = \rho(\mathbf{r}) H_{in}(\mathbf{r}, \mathbf{r}_{in})$  accounts for the amplitude distribution of each virtual source  $\mathbf{r}_{in}$ .  $\mathbf{G}$  is the transmission matrix between

the focal and pupil planes (see Fig. S3). Its elements  $\mathbf{G}(\mathbf{u}_{\text{out}}, \mathbf{r})$  describe the propagation of the wave-field from a point  $\mathbf{r}$  in the MO focal plane to a detector  $\mathbf{u}_{\text{out}}$  in the output pupil plane.

The holy grail for imaging is to have access to this transmission matrix  $\mathbf{G}$ . Its inversion or pseudo-inversion would actually allow to reconstruct a reliable 3D image of the scattering medium, thereby overcoming aberration and multiple scattering effects generated by the medium itself. However, in most imaging configurations, the *true* transmission matrix  $\mathbf{G}$  is not accessible as it would require an invasive measurement. The common assumption in wave imaging, is thus to consider an homogeneous medium model. The free space transmission matrix  $\mathbf{G}_0$  should then be considered. Its elements  $G_0(\mathbf{u}_{\text{out}}, \mathbf{r})$  are simply given by

$$G_0(\mathbf{u}_{\text{out}}, \mathbf{r}) = \frac{1}{j\lambda f} \exp \left[ j \frac{2\pi}{\lambda f} \mathbf{u}_{\text{out}} \cdot \mathbf{r} \right] \quad (3)$$

where  $f$  is the MO's focal length and  $\lambda$  the central wavelength.

In this work, we will use  $\mathbf{G}_0$  as a reference matrix. The columns of  $\mathbf{G}_0$  are actually the reflected wave-fronts that would be obtained in an ideal case, *i.e* without aberrations. Figure 1B compares few examples of reflected wave-fronts (columns of  $\mathbf{R}$ , see Fig. 1B1) with the corresponding ideal wave-fronts (columns of  $\mathbf{G}_0$ , see Fig.1B2). While the latter ones display plane wave fringes whose orientation and spatial frequency is related to the position  $\mathbf{r}_{\text{in}}$  of the input focusing point, the recorded wave-fronts consist in a stack of this geometrical component with a distorted phase component induced by the biological tissues. The key idea of this paper is to isolate the latter contribution by subtracting the recorded wave-front by its ideal counterpart. Mathematically, this operation can be expressed as a Hadamard product between  $\mathbf{R}$  and  $\mathbf{G}_0^*$  (where  $*$  stand for phase conjugate),

$$\mathbf{D} = \mathbf{R} \circ \mathbf{G}_0^* \quad (4)$$

which, in term of matrix coefficients, can be written as

$$D(\mathbf{u}_{\text{out}}, \mathbf{r}_{\text{in}}) = R(\mathbf{u}_{\text{out}}, \mathbf{r}_{\text{in}}) \times G_0^*(\mathbf{u}_{\text{out}}, \mathbf{r}_{\text{in}}) \quad (5)$$

The matrix  $\mathbf{D} = [D(\mathbf{u}_{\text{out}}, \mathbf{r}_{\text{in}})]$  is the so-called distortion matrix. Removing the geometrical component of the reflected wave-field in the pupil plane as done in Eq.4 amounts to shift each virtual source on the optical axis in the focal plane. Physically, this corresponds to a descanned of the reflected light as performed in confocal microscopy.  $\mathbf{D}$  is thus a reflection matrix but with different realizations of virtual sources all located at the origin (see Fig. 2).

The  $\mathbf{D}$ -matrix deduced from  $\mathbf{R}$  is displayed in Fig. 1D1. Compared to  $\mathbf{R}$  (Fig. 1D1), it exhibits both angular and spatial long-scale correlations in the pupil (Fig. 1E3) and focal (Fig. 1E2) planes, respectively. This is also illustrated by examples of distorted wave-fields displayed in Fig. 1B3. While the original reflected wave-fronts did not display any similarity, the distorted component displays similar Fresnel rings whatever the focusing point  $\mathbf{r}_{\text{in}}$ . The  $\mathbf{D}$ -matrix thus reveals input/output correlations of the wave-field that were originally completely hidden in the original  $\mathbf{R}$ -matrix (Fig. 1C).

### Time reversal analysis of the distortion matrix

The next step is to extract and take advantage of those field-field correlations for imaging. To that aim, the spatial correlation matrix  $\mathbf{D}\mathbf{D}^\dagger$  is the adequate tool. It allows to average the distorted wave-field over different realizations of virtual sources and smooth out the source term  $S(\mathbf{r}, \mathbf{r}_{\text{in}})$  in Eq. 2. For spatially-invariant aberrations, the matrix  $\mathbf{D}\mathbf{D}^\dagger$  is actually equivalent to a virtual reflection matrix  $\mathbf{R}'$  that would be recorded for a reflector on the optical axis (27) (see Fig. 2). The reflectivity distribution of this virtual scatterer is given by the mean intensity  $\langle |S(\mathbf{r}, \mathbf{r}_{\text{in}})|^2 \rangle_{\mathbf{r}_{\text{in}}}$  of the virtual sources. Interestingly, for a single reflector, iterative time reversal is shown to converge towards the wave-front that focuses onto the corresponding reflector even through a strong aberrating layer (32). Hence, we are inclined to apply the same process to  $\mathbf{D}\mathbf{D}^\dagger$  in order to retrieve the wave-front that allows to compensate for the aberrations and perfectly focus on the corresponding virtual reflector, *i.e* at the origin of the focal plane.

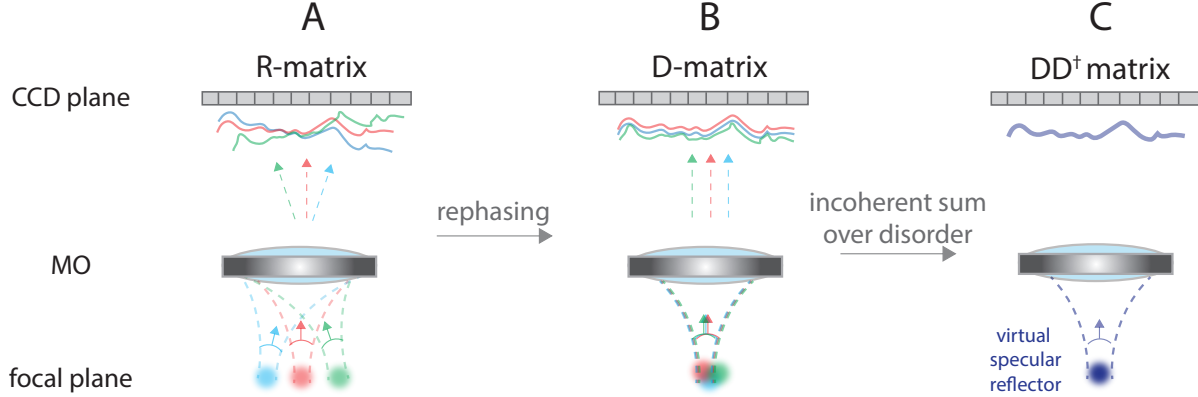


Figure 2: **Synthesizing a virtual reflector from the time reversal analysis of D.** (A) The **R**-matrix contains the wave-fronts induced by each virtual source  $\mathbf{r}_{\text{in}}$ . (B) The removal of the geometric component in each reflected wave-front [Eq.4] amounts to recenter each incident focal spot at the origin:  $S(\mathbf{r}, \mathbf{r}_{\text{in}}) = S(\mathbf{r} - \mathbf{r}_{\text{in}}, \mathbf{r}_{\text{in}})$ . The **D**-matrix corresponds to a set reflected wave-fronts associated with different realizations of the virtual source at the origin. (C) The time reversal operator  $\mathbf{D}\mathbf{D}^\dagger$  allows to smooth out the source term  $S(\mathbf{r} - \mathbf{r}_{\text{in}})$  over those different realizations.  $\mathbf{D}\mathbf{D}^\dagger$  is actually equivalent to a reflection matrix associated with a single virtual specular reflector located at the origin and whose reflectivity distribution is given by  $\langle |S(\mathbf{r} - \mathbf{r}_{\text{in}}, \mathbf{r}_{\text{in}})|^2 \rangle_{\mathbf{r}_{\text{in}}}$ . Iterative time reversal applied to **D** allows to converge towards the time-reversed wave-front  $\mathbf{U}_1^*$  that allows to compensate for aberrations and focus optimally on the virtual reflector.

Unfortunately,  $\mathbf{D}\mathbf{D}^\dagger$  cannot be accessed physically, at least with our experimental set up. Moreover, the aberration is in general spatially-varying and each IP should give rise to a distinct virtual reflector. These issues can be circumvented by noticing that iterative time reversal is mathematically equivalent to a singular value decomposition (SVD) (21, 33). It consists in writing **D** as follows

$$\mathbf{D} = \mathbf{U}\mathbf{\Sigma}\mathbf{V}^\dagger \quad (6)$$

or, in terms of matrix coefficients,

$$D(\mathbf{u}_{\text{out}}, \mathbf{r}_{\text{in}}) = \sum_p \sigma_p U_p(\mathbf{u}_{\text{out}}) V_p^*(\mathbf{r}_{\text{in}}). \quad (7)$$

$\mathbf{\Sigma}$  is a diagonal matrix containing the real positive singular values  $\sigma_i$  in a decreasing order  $\sigma_1 > \sigma_2 > \dots > \sigma_N$ . **U** and **V** are unitary matrices whose columns,  $\mathbf{U}_p = [U_p(\mathbf{u}_{\text{out}})]$  and  $\mathbf{V}_p =$

$[V_p(\mathbf{r}_{\text{in}})]$ , correspond to the output and input singular vectors, respectively. Mathematically, the SVD decomposes a matrix into two subspaces:

- A signal subspace characterized by an important correlation between its lines/columns. The single scattering and forward multiple scattering contributions that manifest a long-range memory effect (12, 34, 35) are expected to lie along this subspace.
- A noise subspace without any correlations between its entries. The spatially-incoherent multiple scattering contribution will lie along this noise subspace. This contribution is associated with multiply-scattered photons that exhibit the same time-of-flight as ballistic photons but whose scattering events take place upstream of the focal plane (30). Note that the experimental noise, in particular the shot noise of the homodyne detection, will also emerge along this subspace.

In the iterative time reversal scheme, the rank of the signal subspace should match, in first approximation, with the number of virtual reflectors, *i.e* here the number of IPs contained in the FOV. Moreover, there shall be a one-to-one association between each virtual reflector and each eigenstate. In other words, each input singular vector  $V_p$  will map onto a different IP in the focal plane while the output singular vector  $U_p$  will yield the corresponding aberration phase law in the pupil plane. Unlike  $\mathbf{R}$  whose rank scales as the number of resolution cells contained in the object (36), the rank of  $\mathbf{D}$  scales as the number of IPs in the FOV.

In the next sections, we will check experimentally all these promising properties of  $\mathbf{D}$  and see how we can take advantage of it for deep imaging.

## Imaging over a single isoplanatic patch

The isoplanatic configuration is first considered by means of the experiment previously described in Fig. 1. Because the aberration is here spatially invariant, the matrix  $\mathbf{D}$  is dominated

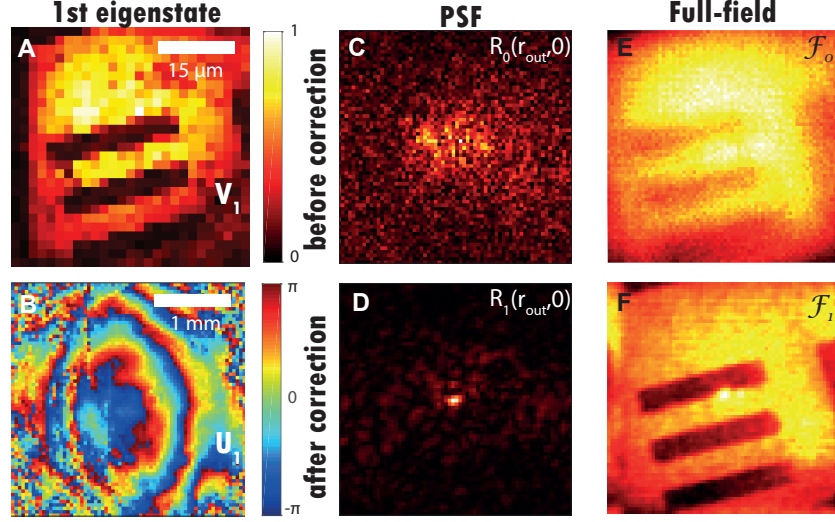


Figure 3: **Imaging through a thick layer of rat intestine tissues.** (A) Modulus of the first input singular vector  $V_1$  of  $D$  in the focal plane. (B) Phase of its first output singular vector  $U_1$  in the pupil plane. (C) Example of PSF deduced from the central column ( $\mathbf{r}_{\text{in}} = \mathbf{0}$ ) of the raw focused matrix  $\mathbf{R}_0$ . (D) Corresponding corrected PSF deduced from the central column of the focused matrix  $\mathbf{R}_1$  (Eq. 9). (E,F) Comparison of the full-field images  $\mathcal{F}_0$  and  $\mathcal{F}$  (Eq. 11) before and after aberration correction.

by a single eigenstate whose singular vectors  $V_1$  and  $U_1$  are displayed in Fig. 3A and B, respectively. The modulus of  $V_1$  displays a contrasted image of the resolution target but its resolution is limited by the low spatial sampling of the illumination scheme. To retrieve a diffraction-limited image, the output singular vector  $U_1$  should be used. Its phase displays the aberration undergone by the reflected wave-front (Fig. 3B). It is made of Fresnel rings mainly induced by the irregular surface of the sample and its index mismatch with the surrounding fluid. The phase of  $U_1$ ,  $\exp(j\arg\{U_1\})$ , can be used to build an estimator  $\hat{G}$  of the transmission matrix between the pupil and focal planes, such that its coefficients read

$$\hat{G}_p(\mathbf{u}_{\text{out}}, \mathbf{r}_{\text{in}}) = \exp(j\arg\{U_p(\mathbf{u}_{\text{out}})\}) G_0(\mathbf{u}_{\text{out}}, \mathbf{r}_{\text{in}}) \quad (8)$$



with  $p = 1$  in the present case. This estimator can be used to project the recorded matrix  $\mathbf{R}$  in the focal basis both at input and output, such that

$$\mathbf{R}_p = \hat{\mathbf{G}}_p^\dagger \mathbf{R} \quad (9)$$

The coefficients  $R_1(\mathbf{r}_{\text{out}}, \mathbf{r}_{\text{in}})$  are the impulse responses between each input focusing point  $\mathbf{r}_{\text{in}}$  and each output imaging point  $\mathbf{r}_{\text{out}}$ . In other words, once reshaped in 2D, each column of  $\mathbf{R}_1$  yields the PSF of the imaging system at the input focusing point  $\mathbf{r}_{\text{in}}$ . The PSF for an input focusing point on the optical axis ( $\mathbf{r}_{\text{in}} = \mathbf{0}$ ) is displayed in Fig. 3D. For sake of comparison, the corresponding initial focal spot is displayed in Fig. 3C. The latter one is extracted from the focused matrix  $\mathbf{R}_0$  deduced from  $\mathbf{R}$  using  $\mathbf{G}_0$ :  $\mathbf{R}_0 = \mathbf{G}_0^\dagger \mathbf{R}$ . While the initial PSF exhibits a random speckle pattern (Fig. 3C), the PSF after correction shows a nearly diffraction-limited focal spot with almost all the energy concentrated in the vicinity of the incident focusing point (Fig. 3D). The characteristic size of the PSF yields the local resolution  $\delta$  of the image at the incident focusing point. Here,  $\delta$  goes from  $15 \mu\text{m}$  on the raw data (Fig. 3C) to  $0.9 \mu\text{m}$  after the matrix correction (Fig. 3D). This value should be compared to the diffraction-limited resolution

$$\delta_{th} = \frac{\lambda}{2n \sin \theta_{max}} \quad (10)$$

with  $\theta_{max} = \mathcal{D}_{out}/(2f)$  the output aperture angle. The numerical application of this formula yields  $\delta_{th} \simeq 0.7 \mu\text{m}$  in our experimental configuration. The mismatch between  $\delta$  and  $\delta_{th}$  comes from the noisy aspect of  $\mathbf{U}_1$  at large spatial frequencies (see Fig. 3B), which prevents from an efficient aberration compensation over the whole aperture angle.

If the spatial sampling was equivalent at input and output, a confocal image could be deduced from the diagonal elements ( $\mathbf{r}_{\text{in}} = \mathbf{r}_{\text{out}}$ ) of  $\mathbf{R}_0$  and  $\mathbf{R}_1$  (22). Here, as a sparse illumination scheme has been employed ( $\delta r_{in} > \delta_{th}$ ), a full-field image is considered and obtained by

summing  $\mathbf{R}$  over its input elements:

$$\mathcal{F}_p(\mathbf{r}_{\text{out}}) = \sum_{\mathbf{r}_{\text{in}}} |R_p(\mathbf{r}_{\text{out}}, \mathbf{r}_{\text{in}})| \quad (11)$$

with  $p = 0$  or  $1$  here. The corresponding images  $\mathcal{F}_0$  and  $\mathcal{F}_1$  are displayed in Figs. 3E and F, respectively. While the patterns of the resolution target are hardly visible on the raw image, the  $\mathbf{D}$ -matrix approach provides a highly contrasted image of the target. To quantify this gain in image quality, the Strehl ratio is a relevant parameter (37). It is defined as the ratio of the PSF peak intensity with and without aberration. Equivalently, it can also be defined in the pupil plane as the squared magnitude of the mean aberration phase factor. Its initial value  $\mathcal{S}_0$  can thus be directly derived from the  $\mathbf{D}$ -matrix coefficients:

$$\mathcal{S}_0 = |\langle \exp(j \arg \{D(\mathbf{u}_{\text{out}}, \mathbf{r}_{\text{in}}) V_1(\mathbf{r}_{\text{in}})\}) \rangle|^2 \quad (12)$$

where the symbol  $\langle \dots \rangle$  denotes an average over  $\mathbf{u}_{\text{out}}$  and  $\mathbf{r}_{\text{in}}$ . In the present case, the original Strehl ratio is  $\mathcal{S}_0 = 8 \times 10^{-5}$ . This experiment corresponds to imaging conditions far from being in the range of operation of conventional AO and explain why the pattern of the resolution target are so hardly visible on the raw image (Fig. 3E). The Strehl ratio  $\mathcal{S}_1$  after the  $\mathbf{U}_1$  correction can be directly extracted from the SVD of  $\mathbf{D}$  (Eq. 7):

$$\mathcal{S}_1 = |\langle \exp(j \arg \{U_1^*(\mathbf{u}_{\text{out}}) D(\mathbf{u}_{\text{out}}, \mathbf{r}_{\text{in}}) V_1(\mathbf{r}_{\text{in}})\}) \rangle|^2 \quad (13)$$

The  $\mathbf{D}$ -matrix correction leads to a Strehl ratio  $\mathcal{S}_1 = 3 \times 10^{-3}$ , thereby improving it by a factor 171. However, Eq. 13 gives the same weight to bright and dark areas of the resolution target in the focal and pupil planes. One possibility is to consider a weighted average instead of Eq.13 by the object reflectivity  $|V_1(\mathbf{r}_{\text{in}})|^2$ . This weighted Strehl ratio  $\mathcal{S}'_1$  then reaches the value of  $1.1 \times 10^{-2}$ . This result is spectacular and accounts for the satisfying image of the resolution target obtained after the  $\mathbf{D}$ -matrix correction (see Fig. 3F).

This first experiment demonstrates the benefit of the  $\mathbf{D}$ -matrix in the simple case of a FOV containing a single IP. In the next section, the case of multiple IPs is tackled.

## Imaging over multiple isoplanatic modes

The first element of the group 6 in the resolution target is now imaged through an aberrating layer consisting in a rough plastic sheet placed  $d = 1$  mm above the resolution target (USAF 1951) (see Fig. 4A). The reflection matrix  $\mathbf{R}$  is measured over a FOV  $F = 57 \times 57 \mu\text{m}^2$  with  $N_{in}=441$  input wave-fronts, a spatial sampling  $\delta r_{in} = 2.85 \mu\text{m}$  and an input pupil aperture  $\mathcal{D}_{in} \times \mathcal{D}_{in} = 1.3 \times 1.3 \text{ mm}^2$ . At the output, the wave-field is recorded over a pupil size of  $\mathcal{D}_{out} \times \mathcal{D}_{out} = 2 \times 2 \text{ mm}^2$  with  $N_{out} = 12321$  pixels and a spatial sampling length  $\delta u_{out}=18 \mu\text{m}$ .

The full-field image  $\mathcal{F}_0$  (Eq. 11) and an example of PSF (Eq. 9) are displayed in Figs. 4A and B, respectively. The PSF is strongly degraded with a characteristic focal spot dimension  $\delta \sim 45 \mu\text{m}$ . This PSF dimension allows to estimate the coherence length  $l_c$  of the aberrating layer. Indeed, under a thin phase screen model,  $l_c$  scales as  $\lambda d / \delta \sim 18 \mu\text{m}$  (38). This parameter  $l_c$  also defines the characteristic size of IPs (38). The number  $Q$  of IPs supported by the FOV can thus be roughly estimated:  $Q \sim (FOV/l_c)^2 \sim 8.5$ .

A  $\mathbf{D}$ -matrix is deduced from  $\mathbf{R}$  (Eq. 4). Its analysis leads to the following estimation of the initial Strehl ratio:  $\mathcal{S}_0 = 2.5 \times 10^{-8}$ . This particularly strong aberration level accounts for the highly blurred aspect of the full-field image in Fig. 4B. This experimental situation is thus particularly extreme, even almost desperate, for a successful imaging of the resolution target. Yet the SVD of  $\mathbf{D}$  will provide the solution.

Fig. 4D displays the histogram of the normalized singular values  $\tilde{\sigma}_i = \sigma_i / \sum_{j=1}^N \sigma_j$ . If recorded data was not corrupted by experimental noise, the matrix would be of effective rank  $Q$ . We could use all the eigenstates of  $\mathbf{D}$  associated with non-zero singular values to retrieve an image of the object. In Fig. 4D, only few singular values seem to emerge from the noise background. Hence, it is difficult to determine the number of eigenstates we need to consider to properly reconstruct an image of the object. This issue can be circumvented by computing the

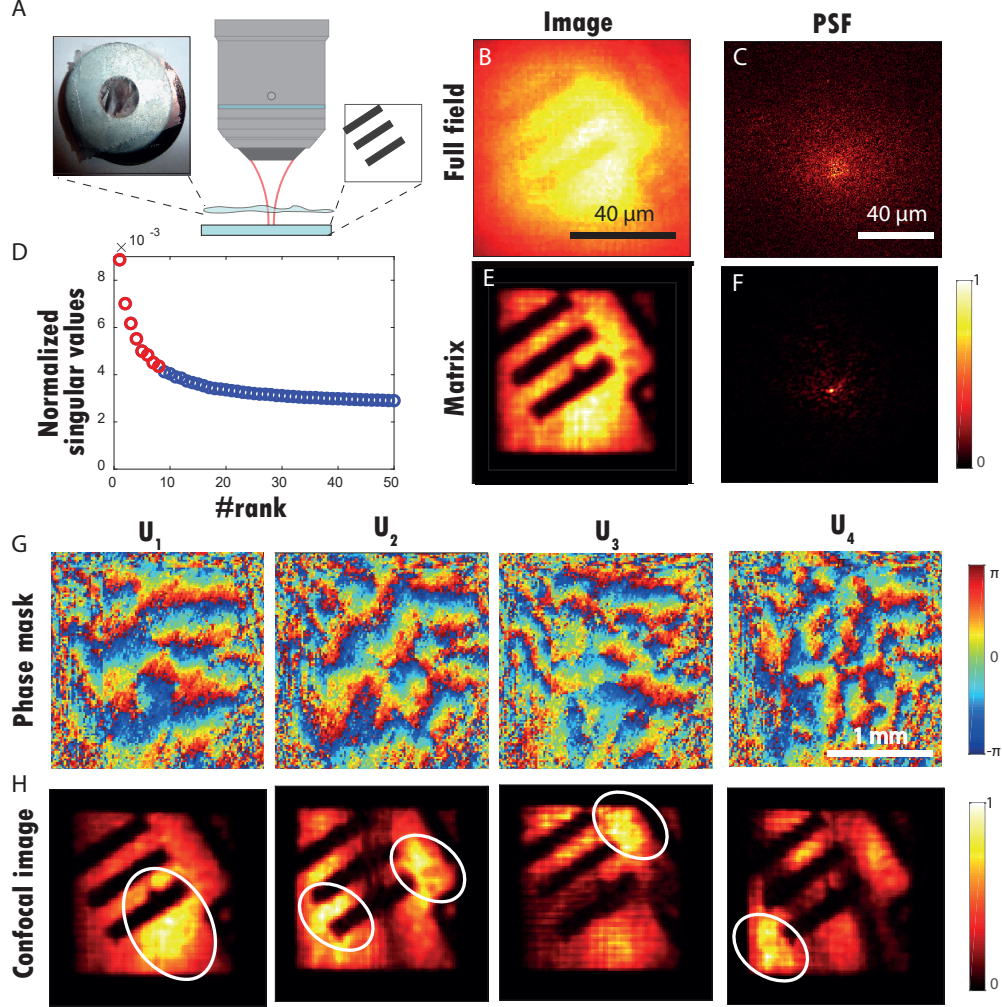


Figure 4: **Matrix imaging through multiple isoplanatic modes.** (A) Schematic of the experiment. A resolution target (USAF 1951) is positioned at a distance  $d = 1$  mm underneath a rough plastic film (see inset). (B) Original full-field image  $\mathcal{F}_0$  (Eq.11). (C) Example of PSF deduced from a column of the raw focused matrix  $\mathbf{R}_0$ . (D) Plot of the normalized singular values  $\tilde{\sigma}_i$  of  $\mathbf{D}$ . The red circles correspond to the eight first singular values (signal subspace), while the noisy singular values are displayed in blue. (E) Matrix image constructed from the eight first eigenstates of  $\mathbf{D}$  (Eq. 16). (F) Example of PSF deduced from a column of the corrected focused matrix  $\mathbf{R}_1$ . (G) Phase of the four first singular vectors  $\mathbf{U}_p$ . (H) Confocal images deduced from the focused reflection matrices  $\mathbf{R}_p$  [Eq.15].

Shannon entropy  $\mathcal{H}$  of the singular values (39, 40), such that

$$\mathcal{H}(\tilde{\sigma}_i) = - \sum_{i=1}^{N_{in}} \tilde{\sigma}_i \log_2 (\tilde{\sigma}_i^2). \quad (14)$$

Shannon entropy delivers the maximally-noncommittal data set at a given signal-to-noise ratio, that is to say, the most information with the least artifact. The Shannon entropy can be used as an indicator of how many eigenstates are needed to build an adequate image of the object without being affected by experimental noise.

The singular values of Fig. 4D have an entropy  $\mathcal{H} \simeq 8.4$ . Hence, only the eight first singular states shall be considered. Fig. 4G displays the phase of the four first singular vectors  $\mathbf{U}_i$  in the pupil plane. They display phase distortions whose typical coherence length  $u_c$  scales as  $fl_c/d \sim 100 \mu\text{m}$ . The phase conjugation of these singular vectors should compensate for the detrimental effect of the aberrating layer in different parts of the FOV. A set of focused reflection matrices  $\mathbf{R}_p$  can be deduced (Eq.9). Fig. 4f displays an example of corrected PSF extracted from a column of  $\mathbf{R}_1$ . Its comparison with the original PSF in Fig. 4C shows how the phase conjugation of  $\mathbf{U}_1$  allows to compensate for the aberrations at this incident focusing point. On the one hand, the PSF width is narrowed by a factor 20, going from  $\delta \sim 45 \mu\text{m}$  to  $2.25 \mu\text{m}$ . The latter value should be compared with the diffraction-limited resolution  $\delta_{th} \sim 2 \mu\text{m}$  (Eq. 10) in our experimental conditions. The Strehl ratio is increased by a factor  $2.2 \times 10^3$ , going from  $\mathcal{S}'_0 = 1.6 \times 10^{-6}$  (Eq. 12) to  $\mathcal{S}'_1 = 3.5 \times 10^{-3}$  (Eq. 13).

Confocal images can be deduced from the focused reflection matrices  $\mathbf{R}_p$ :

$$\mathcal{I}_p(\mathbf{r}_{out}) = \sum_{\mathbf{r}_{in}} |R_p(\mathbf{r}_{out}, \mathbf{r}_{in})| e^{-\|\mathbf{r}_{out} - \mathbf{r}_{in}\|^2 / 2l_p^2} \quad (15)$$

where  $l_p$  is the aperture of the numerical confocal pinhole (22). This finite aperture allows to average the output image over neighbour incident focusing points in order to smooth out the sparse illumination. Figure 4H displays the confocal images  $\mathcal{I}_p$  for  $l_p = 2 \mu\text{m}$ . Each singular

vector  $\mathbf{U}_p$  is associated with distinct IPs. For a specular object such as a resolution target, the SVD of  $\mathbf{D}$  has indeed the property of decomposing the FOV into a set of isoplanatic modes of spatial extent  $l_c$ . Their shape depends on the auto-correlation function of the aberrating phase screen. For exponential or sinc models, the FOV would be decomposed into sinusoidal wave functions (41) analogous to optical fiber modes or to prolate spheroidal wave functions (36), respectively. Here, the autocorrelation function of the aberrating phase displays a Gaussian-like shape. The FOV is thus mapped onto Hermite-Gaussian wave functions analogous to laser cavity modes (42).

A final image  $\mathcal{I}$  of the resolution target can be obtained by summing the previous isoplanatic modes  $\mathcal{I}_p$ :

$$\mathcal{I}(\mathbf{r}_{\text{out}}) = \sum_{p=1}^{\mathcal{H}(\tilde{\sigma}_i)} \mathcal{I}_p(\mathbf{r}_{\text{out}}). \quad (16)$$

The final result is displayed in Fig. 4E. The comparison with the initial full-field image (Fig. 4B) illustrates the benefit of the  $\mathbf{D}$ –matrix approach. Spatially-varying aberrations are overcome and a contrasted image of the resolution target is recovered over the whole FOV. This experiment demonstrates how the  $\mathbf{D}$ –matrix allows to decompose the FOV into several isoplanatic modes and map each of them onto orthonormal distorted phase laws. However, this demonstration has been restricted to the case of a 2D aberrating phase layer. In the next section, we consider the case of a cornea with compromised transparency as a three-dimensional aberrating and scattering structure.

## Imaging through an opaque cornea

The experimental configuration is displayed in Fig. 5A. The number “3” of the group 5 in the resolution target is imaged through a 700- $\mu\text{m}$ -thick edematous non-human primate cornea. The reflection matrix  $\mathbf{R}$  is measured over a FOV  $F = 52 \times 52 \mu\text{m}^2$  by means of  $N_{in}=625$  input wave-fronts, a spatial sampling  $\delta r_{in} = 2.1 \mu\text{m}$  and an input pupil aperture  $\mathcal{D}_{in} \times \mathcal{D}_{in} = 1 \times 1$

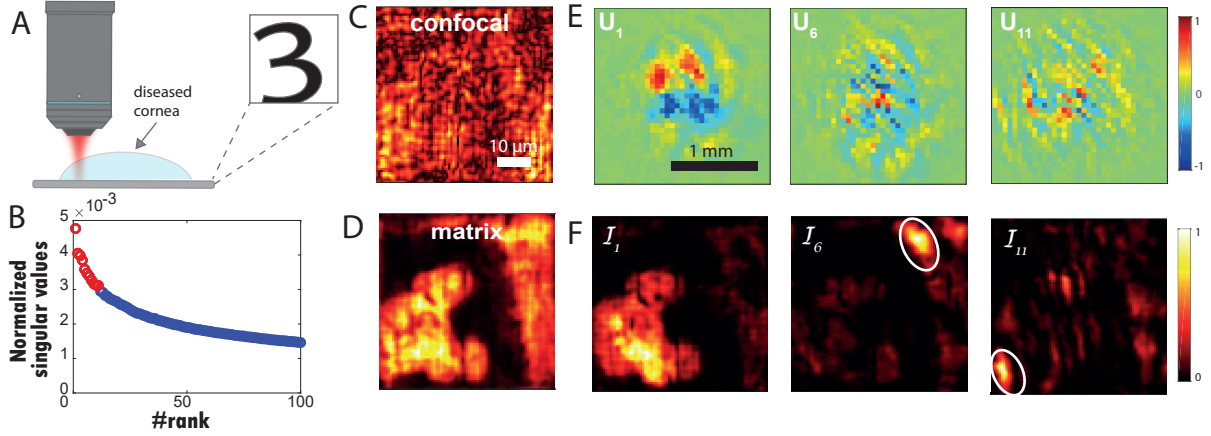


Figure 5: **Imaging through a cornea with compromised transparency.** (A) Schematic of the experiment. A resolution target (USAF 1951) is positioned below a non-human primate cornea (see inset). (B) Plot of the normalized singular values  $\tilde{\sigma}_i$  of  $\mathbf{D}$ . The red circles correspond to the eleven first singular values (signal subspace), while the noisy singular values are displayed in blue. (C) Original confocal image deduced from the focused reflection matrix  $\mathbf{R}_0$  (Eq. 15). (D) Final matrix image constructed from the eleven first eigenstates of  $\mathbf{D}$  (Eq. 16). (E) Real parts of  $\mathbf{U}_1$ ,  $\mathbf{U}_6$  and  $\mathbf{U}_{11}$ . (F) Corresponding confocal images deduced from the focused reflection matrices  $\mathbf{R}_p$  (Eq. 15).

$\text{mm}^2$ . At the output, the wave-field is recorded over an output pupil size  $\mathcal{D}_{out} \times \mathcal{D}_{out} = 2 \times 2 \text{ mm}^2$  with  $N_{out} = 1296$  pixels and a spatial sampling length  $\delta u_{out} = 56 \mu\text{m}$ . Fig. 5C displays the confocal image  $\mathcal{I}_0$  deduced from  $\mathbf{R}_0$  with  $l_p = 1 \mu\text{m}$  (Eq. 15). Multiple scattering and aberrations induced by the cornea induce a random speckle reflected wave-field that prevents from imaging the resolution target. On the contrary, as we will see, the  $\mathbf{D}$ -matrix analysis allows to nicely recover the pattern “3” of the resolution target (see Fig. 5D).

Fig. 5C displays the spectrum of the singular values  $\tilde{\sigma}_i$ . The first singular value emerges from the rest of the spectrum but it is difficult to know until which rank the eigenstates can be considered as belonging to the signal subspace. As previously, the Shannon entropy of the singular values yields an unambiguous answer:  $\mathcal{H}(\sigma_i) = 10.7$ . The 11<sup>th</sup> first singular states should thus be considered. Fig. 5E displays the 1<sup>st</sup>, 6<sup>th</sup> and 11<sup>th</sup> singular vectors  $\mathbf{U}_i$  in the

pupil plane. The complexity of the wave-front distortion, *i.e* their spatial frequency content, increases with the rank of the corresponding singular values. The corresponding isoplanatic modes  $\mathcal{I}_p$  (Eq. 15) are displayed in Fig. 5F. While the first singular vector  $\mathbf{U}_1$  allows a wide-field correction of low-order aberration, the higher rank singular vectors are associated with high-order aberrations that are effective over smaller isoplanatic modes. In Fig. 5D, the whole spatial frequency spectrum of wave-front distortions is finally compensated by smartly combining the confocal images  $\mathcal{I}_p$  associated with each singular state from  $\mathbf{D}$ 's signal subspace (Eq.16). The comparison of the initial (Fig. 5C) and final (Fig. 5D) images is spectacular with a Strehl ratio gain  $\mathcal{S}'_1/\mathcal{S}'_0 = 230$ . The comparison of  $\mathcal{I}$  (Fig. 5D) and  $\mathcal{I}_1$  (see the first inset of Fig. 5F) illustrates the benefit of a matrix approach of aberration correction compared to conventional AO, since the latter one would yield  $\mathcal{I}_1$  in theory.

This decomposition of complex aberration phase laws over a set of isoplanatic modes opens important perspectives for aberrometry. It actually goes well beyond state-of-the-art techniques that basically consist in a simple projection over a set of Zernike polynomials. Moreover, an estimator of the single-to-multiple scattering (SMR) ratio can be built on the relative energy between the signal and noise sub-spaces of  $\mathbf{D}$ :

$$\text{SMR} = \frac{\sum_{i=1}^{\mathcal{H}(\sigma_i)} \sigma_i^2}{\sum_{i=\mathcal{H}(\sigma_i)+1}^{N_{in}} \sigma_i^2}. \quad (17)$$

The SMR can actually be a quantitative bio-marker of the corneal opacity. Based on a fit with a recent analytical study of the SMR (30), the cornea thickness  $L$  can be estimated in terms of scattering mean free path  $\ell_s$ :  $L \sim 10\ell_s$ . As the cornea thickness is known ( $L = 700 \mu\text{m}$ ), the scattering mean free path can be deduced:  $\ell_s \sim 70 \mu\text{m}$ . Interestingly, this value is in excellent agreement with recent *in-vivo* measurements of  $\ell_s$  in pathological cornea with compromised transparency (?). This value of  $10\ell_s$  for the cornea thickness highlights the difficult experimental conditions under which the imaging of the resolution target has been successfully achieved.



In conclusion, this last experiment shows all the potential of a matrix approach for eye aberrometry and opacimetry. Of course, this method is by no means limited to eye diagnosis. It can be applied to the characterization of any kind of biological tissues provided that we have access to the associated reflection matrix.

## DISCUSSION

In this article, we present a novel and non-invasive method for aberration compensation in optical coherence microscopy. This approach relies on the measurement of the reflected wave-field in the Fourier space for a set of focused illuminations that act as virtual sources in the focal plane. Based on a decomposition of the output field in the Fourier space, a new operator, the so-called distortion matrix, is built. It connects each virtual source with the distorted component of the wave-field induced in the pupil plane. By studying the spatial and angular correlations of this operator through an SVD, we demonstrate the efficient compensation of both low- and high-order aberrations over multiple IPs. This is in contrast with most AO techniques whose range of operation is limited to a single IP. Multi-conjugate AO can potentially overcome this issue but this is at the price of a much more complex optical set up (44, 45). Here our imaging device is relatively simple as high-order aberration are corrected over multiple IPs in post-processing. This is also a clear improvement compared to the CLASS method developed by Kang *et al.* (25, 26). The CLASS approach consists in optimizing the correlations of the reflected wave-field from the far-field. Its field-of-operation is thus limited to a single IP. On the contrary, our matrix analysis is dual (focal/pupil planes) and the case of multiple IPs can be tackled. Moreover, our approach relies on the Shannon entropy that provides an objective criterion to determine the number of isoplanatic modes supported by the FOV.

Besides aberration correction, our approach leverages the correlations of the output wave-field to get rid of the multiple scattering background. The latter contribution is actually spatially

incoherent. It thus mainly lies along the noise subspace of the  $\mathbf{D}$ —matrix. Thanks to these features, we were able to image through 10 scattering mean free paths of biological tissues, which is beyond the imaging depth of conventional OCT systems (30). Compared to the previously developed smart-OCT method that was able to detect few bright scatterers at large penetration depth ( $12\ell_s$ ) (22), the  $\mathbf{D}$ —matrix approach yields a direct image of the sample reflectivity at a diffraction-limited resolution.

This operator thus opens a new route towards real-time deep optical imaging of biological tissues. In that respect, the experimental set up and procedure used in this paper are clearly perfectible. In particular, the scanning illumination scheme was not optimized because of the SLM speed. We counteracted this issue with a sparse illumination. However, this in return limited the available number of angular degrees of freedom at the input, which prevents us from an aberration correction at the input. The use of a galvanometric mirror or an high-speed deformable mirror would reduce drastically the acquisition time. Another possibility would be to switch from a scanning to a full-field illumination scheme. A measurement of the coherent reflection matrix  $\mathbf{R}$  can be performed under a spatially incoherent illumination (46, 47). This full-field configuration would allow to record the  $\mathbf{R}$ — and  $\mathbf{D}$ —matrices over millimetric volumes in a moderate acquisition time.

Finally, although the use of a resolution target was important for the present proof-of-concept, a direct imaging of biological specimens over large penetration depth will be the next step. The  $\mathbf{D}$ —matrix concept is actually not limited to deterministic objects in a specular reflection regime. Strikingly, it performs even better in three-dimensional scattering structures of random reflectivity. The randomness of the object actually smooths out more efficiently the virtual source term of Eq.2. Input and output transfer functions of the imaging system can then be independently and precisely extracted. The aberration correction can be then applied both at input and output (26), leading to sub-diffraction resolution (48) as in an ideal confocal imaging

apparatus. The ability of identifying multiple IPs is also particularly promising to map the specimen induced-aberration. A quantitative aberrometer and/or opacimeter are actually important diagnosis tools especially in the context of retinal imaging (49).

In summary, we have introduced, in this work, a new operator, the so-called distortion matrix  $\mathbf{D}$ , which reveals the hidden correlations of the reflected wave-field. This matrix results from the mismatch between the phase of the recorded reflection matrix and those of a reference matrix that would be obtained in an ideal configuration. As shown in this paper,  $\mathbf{D}$  gives access to the non-invasive transmission matrix between each sensor and each voxel of the field-of-view. Then, by solving the corresponding inverse problem, an image of scattering sample can be obtained as if the medium ahead was made transparent. The  $\mathbf{D}$ -matrix concept is very general. First, it can be extended to any kind of waves and experimental configurations for which a measurement of the amplitude and phase of the reflected wave-field is possible under multiple illumination (34,35,50). Second, its definition is very flexible as the reference matrix can evolve according to our degree of prior knowledge of the inspected medium. This  $\mathbf{D}$ -matrix concept thus opens a new route towards a global and non-invasive matrix approach of deep imaging in biological tissues.

## MATERIALS AND METHODS

### Experimental set up

The experimental configuration is identical to the one described in (22) except for the MO that had been replaced by a water immersion one. The following component were used in the experimental setup (see Fig. S1): a femtosecond laser (Femtosecond Fusion 20-400), an SLM (PLUTONIR-2, HOLOEYE), an objective lens (40 $\times$ ; NA, 0.8; Olympus), and a CCD camera (Dalsa Pantera 1M60) with a dynamic range of 60 dB. The incident light power in the back pupil plane of the MO was 10 mW in the experiment. Thus, the radiant flux was  $10^6$  W/cm<sup>2</sup> at

the focal spot in free space. For each input wave-front, the complex-reflected wave field was extracted from four intensity measurements using phase shifting interferometry.

## Image acquisition and data analysis

Both acquisition and analysis of data were performed using Matlab custom-written codes. This codes are available from the authors upon request.

## SUPPLEMENTARY MATERIALS

Fig. S1. Measuring the time-gated reflection matrix.

Fig. S2. Building the reflection matrix  $R$ .

Fig. S3. Modeling the propagation of light from the input virtual source plane to the output pupil plane.

## REFERENCES AND NOTES

### References

1. H. W. Babcock, The possibility of compensating astronomical seeing. *Publications of the Astronomical Society of the Pacific* **65**, 229–236 (1953).
2. R. Foy, A. Labeyrie, Feasibility of adaptive telescope with laser probe. *A&A* **152**, L29–L31 (1985).
3. S. T. Thurman, J. R. Fienup, Correction of anisoplanatic phase errors in digital holography. *J. Opt. Soc. Am. A* **25**, 995–999 (2008).
4. A. E. Tippie, J. R. Fienup, Multiple-plane anisoplanatic phase correction in a laboratory digital holography experiment. *Opt. Lett.* **35**, 3291–3293 (2010).

5. M. J. Booth, M. A. Neil, R. Juškaitis, T. Wilson, Adaptive aberration correction in a confocal microscope. *Proc. Natl. Acad. Sci. USA* **99**, 5788–5792 (2002).
6. X. Tao, B. Fernandez, O. Azucena, M. Fu, D. Garcia, Y. Zuo, D. C. Chen, J. Kubby, Adaptive optics confocal microscopy using direct wavefront sensing. *Optics letters* **36**, 1062–1064 (2011).
7. D. Débarre, E. J. Botcherby, T. Watanabe, S. Srinivas, M. J. Booth, T. Wilson, Image-based adaptive optics for two-photon microscopy. *Opt. Lett.* **34**, 2495–2497 (2009).
8. N. Ji, D. E. Milkie, E. Betzig, Adaptive optics via pupil segmentation for high-resolution imaging in biological tissues. *Nat. Methods* **7**, 141–147 (2010).
9. I. N. Papadopoulos, J.-S. Jouhanneau, J. F. Poulet, B. Judkewitz, Scattering compensation by focus scanning holographic aberration probing (f-sharp). *Nat. Photonics* **11**, 116–123 (2017).
10. B. Hermann, E. Fernández, A. Unterhuber, H. Sattmann, A. Fercher, W. Drexler, P. Prieto, P. Artal, Adaptive-optics ultrahigh-resolution optical coherence tomography. *Opt. Lett.* **29**, 2142–2144 (2004).
11. S. G. Adie, B. W. Graf, A. Ahmad, P. S. Carney, S. A. Boppart, Computational adaptive optics for broadband optical interferometric tomography of biological tissue. *Proc. Natl. Acad. Sci. USA* **109**, 7175–7180 (2012).
12. B. Judkewitz, R. Horstmeyer, I. M. Vellekoop, I. N. Papadopoulos, C. Yang, Translation correlations in anisotropically scattering media. *Nat. Phys.* **11**, 684–689 (2015).
13. M. Minsky, Confocal scanning microscope (1955).

14. M. R. Hee, E. A. Swanson, J. G. Fujimoto, J. A. Izatt, Femtosecond transillumination tomography in thick tissues. *Opt. Lett.* **18**, 1107–1109 (1993).
15. I. M. Vellekoop, A. P. Mosk, Focusing coherent light through opaque strongly scattering media. *Opt. Lett.* **32**, 2309–2311 (2007).
16. S. M. Popoff, G. Lerosey, R. Carminati, M. Fink, A. C. Boccara, S. Gigan, Measuring the Transmission Matrix in Optics: An Approach to the Study and Control of Light Propagation in Disordered Media. *Phys. Rev. Lett.* **104**, 100601 (2010).
17. S. M. Popoff, G. Lerosey, M. Fink, A. C. Boccara, S. Gigan, Image transmission through an opaque material. *Nat. Commun.* **1**, 1–5 (2010).
18. M. Kim, Y. Choi, C. Yoon, W. Choi, J. Kim, Q.-H. Park, W. Choi, Maximal energy transport through disordered media with the implementation of transmission eigenchannels. *Nature Photon.* **6**, 583–587 (2012).
19. T. Cizmar, K. Dholakia, Exploiting multimode waveguides for pure fibre- based imaging. *Nat. Commun.* **3** (2012).
20. I. N. Papadopoulos, S. Farahi, C. Moser, D. Psaltis, Focusing and scanning light through a multimode optical fiber using digital phase conjugation. *Opt. Exp.* **20**, 10583–10590 (2012).
21. S. M. Popoff, A. Aubry, G. Lerosey, M. Fink, A. C. Boccara, S. Gigan, Exploiting the time-reversal operator for adaptive optics, selective focusing, and scattering pattern analysis. *Phys. Rev. Lett.* **107**, 263901 (2011).
22. A. Badon, D. Li, G. Lerosey, A. C. Boccara, M. Fink, A. Aubry, Smart optical coherence tomography for ultra-deep imaging through highly scattering media. *Sci. Adv.* **2**, e1600370 (2016).

23. Y. Choi, T. R. Hillman, W. Choi, N. Lue, R. R. Dasari, P. T. C. So, W. Choi, Z. Yaqoob, Measurement of the time-resolved reflection matrix for enhancing light energy delivery into a scattering medium. *Phys. Rev. Lett.* **111**, 243901 (2013).
24. S. Jeong, Y.-R. Lee, W. Choi, S. Kang, J. H. Hong, J.-S. Park, Y.-S. Lim, H.-G. Park, W. Choi, Focusing of light energy inside a scattering medium by controlling the time-gated multiple light scattering. *Nature Photon.* **12**, 277–283 (2018).
25. S. Kang, S. Jeong, W. Choi, H. Ko, T. D. Yang, J. H. Joo, J.-S. Lee, Y.-S. Lim, Q.-H. Park, W. Choi, Imaging deep within a scattering medium using collective accumulation of single-scattered waves. *Nature Photonics* **9**, 253–258 (2015).
26. S. Kang, P. Kang, S. Jeong, Y. Kwon, T. D. Yang, J. H. Hong, M. Kim, K.-D. Song, J. H. Park, J. H. Lee, *et al.*, High-resolution adaptive optical imaging within thick scattering media using closed-loop accumulation of single scattering. *Nat. Commun.* **8**, 2157 (2017).
27. J.-L. Robert, M. Fink, Green's function estimation in speckle using the decomposition of the time reversal operator: Application to aberration correction in medical imaging. *J. Acoust. Soc. Am.* **123**, 866-877 (2008).
28. J.-L. Robert, M. Fink, The time-reversal operator with virtual transducers: Application to far-field aberration correction. *J. Acoust. Soc. Am.* **124**, 3659-3668 (2008).
29. S. Jacques, Optical properties of biological tissues: a review. *Phys. Med. Biol.* **58**, R37-R61 (2013).
30. A. Badon, A. C. Boccara, G. Lerosey, M. Fink, A. Aubry, Multiple scattering limit in optical microscopy. *Opt. Exp.* **25**, 28914–28934 (2017).
31. See Supplemental Material at ... for examples of image construction ...

32. C. Prada, M. Fink, Eigenmodes of the time reversal operator: A solution to selective focusing in multiple-target media. *Wave Motion* **20**, 151–163 (1994).
33. C. Prada, J.-L. Thomas, Experimental subwavelength localization of scatterers by decomposition of the time reversal operator interpreted as a covariance matrix. *J. Acoust. Soc. Am.* **114**, 235–243 (2003).
34. A. Aubry, A. Derode, Random Matrix Theory Applied to Acoustic Backscattering and Imaging In Complex Media. *Phys. Rev. Lett.* **102**, 084301 (2009).
35. S. Shahjahan, A. Aubry, F. Rupin, B. Chassignole, A. Derode, A random matrix approach to detect defects in a strongly scattering polycrystal: How the memory effect can help overcome multiple scattering. *Appl. Phys. Lett.* **104**, 234105 (2014).
36. J.-L. Robert, M. Fink, The prolate spheroidal wave functions as invariants of the time reversal operator for an extended scatterer in the fraunhofer approximation. *J. Acoust. Soc. Am.* **125**, 218–226 (2009).
37. V. N. Mahajan, Strehl ratio for primary aberrations: some analytical results for circular and annular pupils. *J. Opt. Soc. Am.* **72**, 1258–1266 (1982).
38. J. Mertz, H. Paudel, T. G. Bifano, Field of view advantage of conjugate adaptive optics in microscopy applications. *Appl. Opt.* **54**, 3498–3506 (2015).
39. L. L. Campbell, Minimum coefficient rate for stationary random processes. *Inf. Control* **3**, 360–371 (1960).
40. S. J. Roberts, W. Penny, L. Rezek, Temporal and spatial complexity measures for electroencephalogram based brain-computer interfacing. *Med. Biol. Eng. Comput.* **37**, 93–98 (1999).



41. R. G. Ghanem, R. D. Spanos, *Stochastic Finite Elements: A Spectral Approach* (Springer-Verlag, New York, 1991).
42. A. Aubry, J. de Rosny, J.-G. Minonzio, C. Prada, M. Fink, Gaussian beams and legendre polynomials as invariants of the time reversal operator for a large rigid cylinder. *J. Acoust. Soc. Am.* **120**, 2746-2754 (2006).
43. B. Riviere, Objective and quantitative analysis of corneal transparency with clinical (in vivo) imaging technology, Master's thesis, School of Engineering Sciences, KTH Royal Institute of Technology, Sweden (2018).
44. Z. Kam, P. Kner, D. Agard, J. W. Sedat, Modelling the application of adaptive optics to wide-field microscope live imaging. *J. Microscopy* **226**, 33–42 (2007).
45. R. D. Simmonds, M. J. Booth, Modelling of multi-conjugate adaptive optics for spatially variant aberrations in microscopy. *J. Opt.* **15**, 094010 (2013).
46. A. Badon, G. Lerosey, A. C. Boccara, M. Fink, A. Aubry, Retrieving time-dependent green's functions in optics with low-coherence interferometry. *Phys. Rev. Lett.* **114**, 023901 (2015).
47. A. Badon, D. Li, G. Lerosey, A. C. Boccara, M. Fink, A. Aubry, Spatio-temporal imaging of light transport in highly scattering media under white light illumination. *Optica* **3**, 1160–1166 (2016).
48. C. J. Sheppard, Super-resolution in confocal imaging. *Optik* **80**, 53–54 (1988).
49. V. Mazlin, P. Xiao, E. Dalimier, K. Grieve, K. Irsch, J.-A. Sahel, M. Fink, A. C. Boccara, In vivo high resolution human corneal imaging using full-field optical coherence tomography. *Biomed. Opt. Exp.* **9**, 557–568 (2018).

50. T. Blondel, J. Chaput, A. Derode, M. Campillo, A. Aubry, Matrix approach of seismic imaging: Application to the erebus volcano, antarctica. *J. Geophys. Res.: Solid Earth* **123**, 10–936 (2018).

## Acknowledgements

**Funding:** The authors are grateful for the funding provided by Labex WIFI (Laboratory of Excellence within the French Program Investments for the Future) (ANR-10-LABX-24 and ANR-10-IDEX-0001-02 PSL\*). A.B. acknowledges financial support from the French “Direction Générale de l’Armement” (DGA). This project has received funding from the European Research Council (ERC) under the European Union’s Horizon 2020 research and innovation programme (grant agreements No. 610110 and No. 819261). K.I. acknowledges financial support from the European Union’s Horizon 2020 research and innovation programme under the Marie Skłodowska-Curie grant agreement No. 709104.

**Author Contributions** A.A. initiated and supervised the project. A.B. built the experimental setup and performed the experiments. A.B., V.B., and A.A. analyzed the experiments. V.B. and A.A. performed the theoretical study. A.B. and A.A. prepared the manuscript. A.B., V.B., K.I., A.C.B., M.F., and A.A. discussed the results and contributed to finalizing the manuscript.

**Competing Interests** The authors declare that they have no competing financial interests.

**Data and materials availability:** All data needed to evaluate the conclusions in the paper are present in the paper and/or the Supplementary Materials. Additional data related to this paper may be requested from the authors.

## SUPPLEMENTARY FIGURES

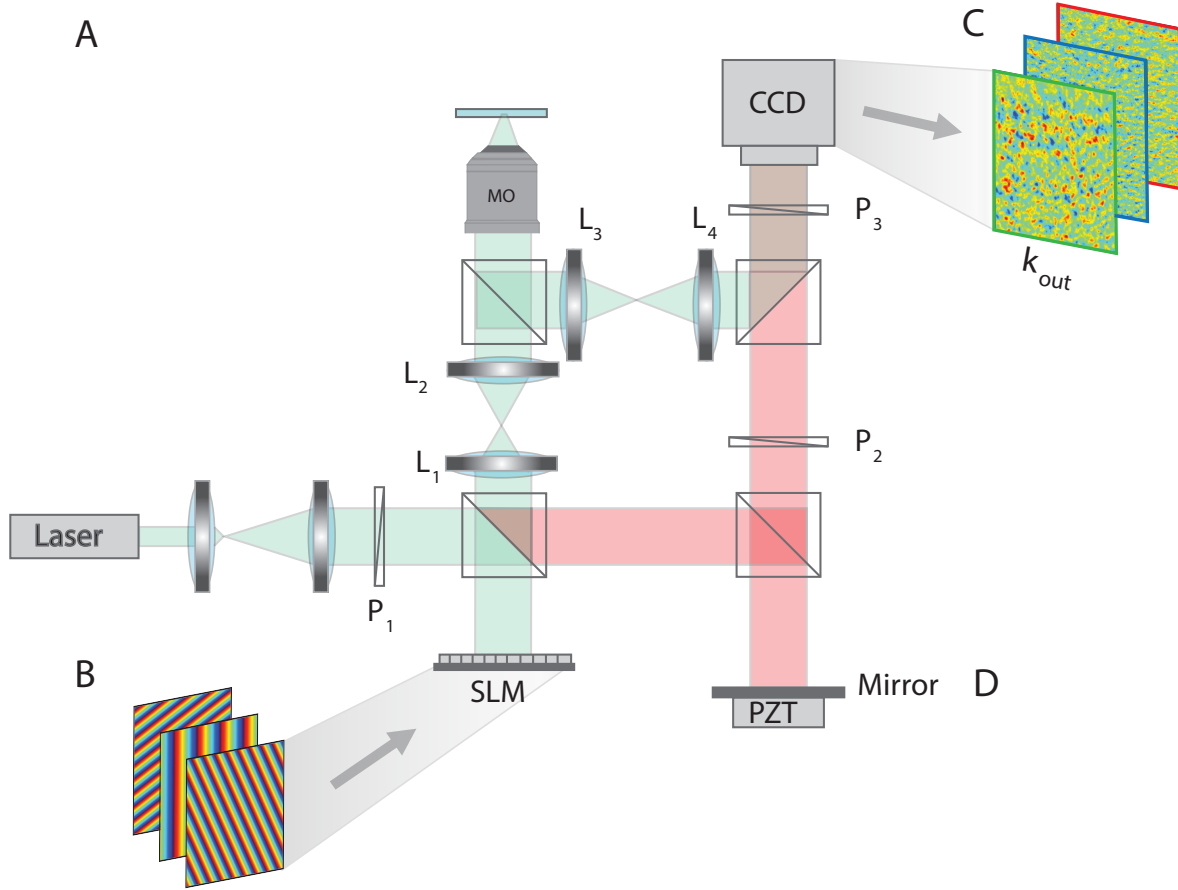


Figure S1: **Measuring the time-gated reflection matrix.** Experimental set up: P: polarizer, MO: microscope objective, BS: beam splitter, PBS: polarized beam splitter, SLM : spatial light modulator, PZT: piezo phase shifter, M: Mirror. A femtosecond laser beam (center wavelength: 810 nm, bandwidth: 40 nm) is shaped by an SLM acting as a diffraction grating. A set of incident plane waves is thus emitted from the SLM and focused at a different position in the focal plane of a MO (NA=0.4). The backscattered wave-field is collected through the same MO and interferes with a reference beam on a CCD camera. The latter one is conjugated with the back focal plane of the MO. The amplitude and phase of the wave-field is recorded by phase shifting interferometry (16). The time of flight  $t$  is controlled by the length of the interferometric arm and is matched with the position of the focal plane. For each input focusing point  $\mathbf{r}_{in}$ , a reflected wave-field is recorded in the pupil plane and stored along a column vector in the matrix  $\mathbf{R}) = [R(\mathbf{u}_{out}, \mathbf{r}_{in})]$ .

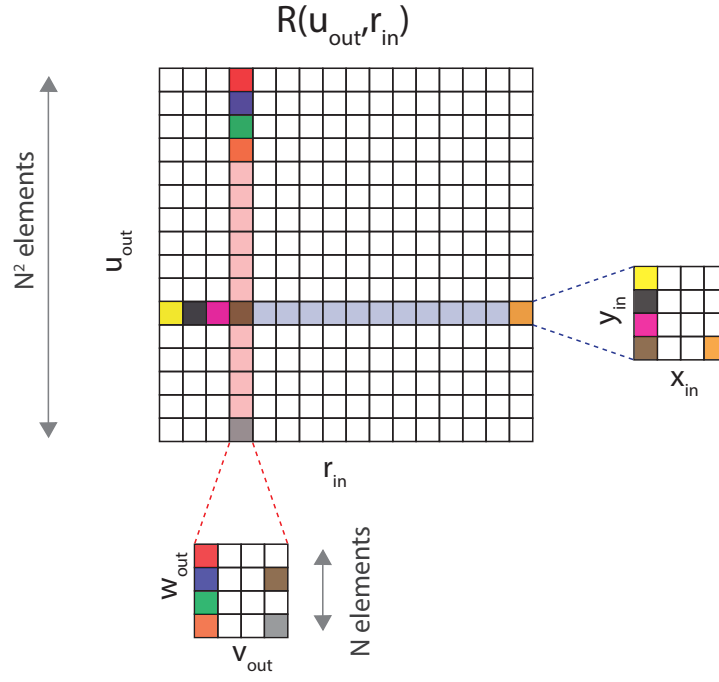


Figure S2: **Building the reflection matrix  $\mathbf{R}$ .** For each focused illumination at  $\mathbf{r}_{\text{in}} = (x_{\text{in}}, y_{\text{in}})$ , the reflected wave-field  $\psi_{\mathbf{r}_{\text{in}}}(v_{\text{out}}, w_{\text{out}})$  is recorded in the pupil plane by each pixel of the CCD camera whose position is denoted by the vector  $\mathbf{u}_{\text{out}} = (v_{\text{out}}, w_{\text{out}})$ . Each wave-field is concatenated and stored along a column vector. This set of column vectors forms the reflection matrix  $\mathbf{R} = [R(\mathbf{u}_{\text{out}}, \mathbf{r}_{\text{in}})]$ , such that  $R(\mathbf{u}_{\text{out}}, \mathbf{r}_{\text{in}}) = \psi_{\mathbf{r}_{\text{in}}}(v_{\text{out}}, w_{\text{out}})$ .

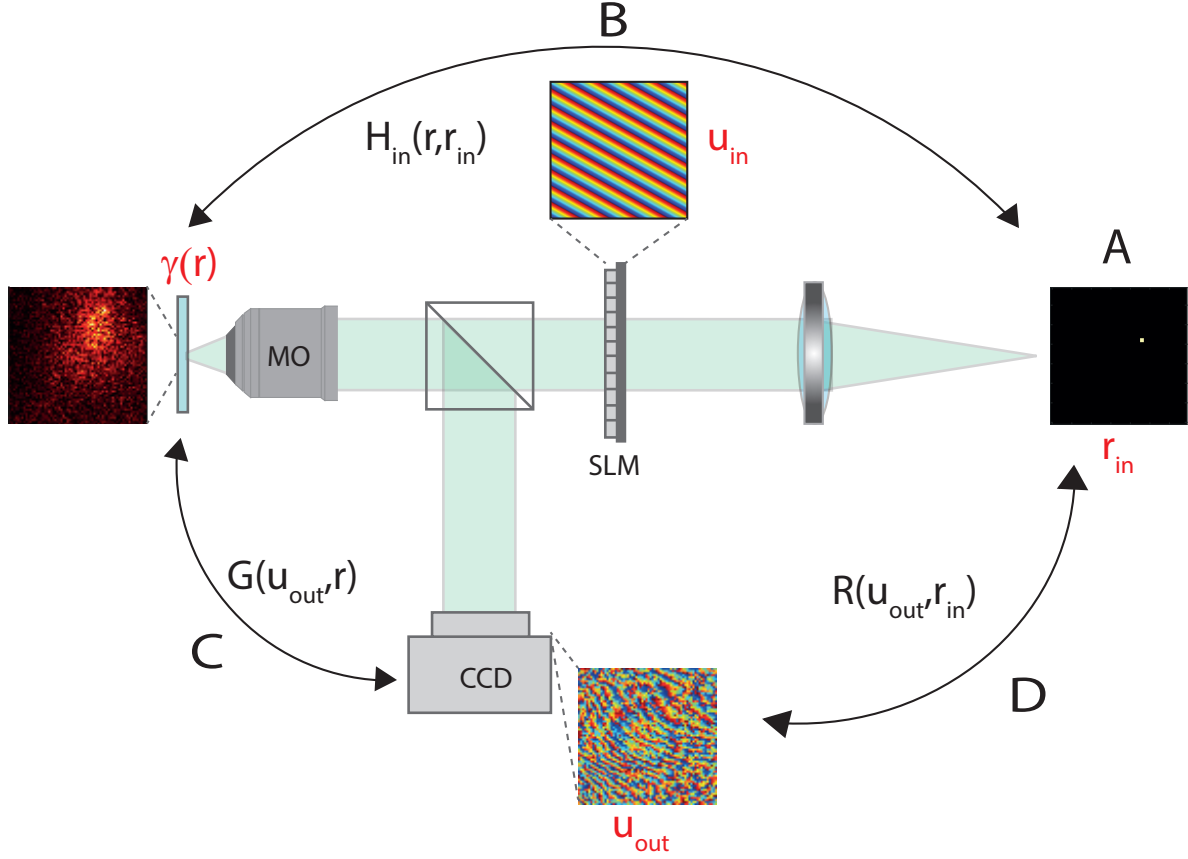


Figure S3: **Modeling the propagation of light from the input virtual source plane to the output pupil plane.** The reflection matrix  $\mathbf{R}$  contains the impulse responses  $R(\mathbf{u}_{\text{out}}, \mathbf{r}_{\text{in}})$  between each virtual source point  $\mathbf{r}_{\text{in}}$  and each CCD pixel  $\mathbf{u}_{\text{out}}$  in the output pupil plane. (A) The virtual source point  $\mathbf{r}_{\text{in}}$  is produced by each transverse mode shaped by the SLM in the input pupil plane. (B) The propagation between the virtual source plane and the focal plane of the MO can be modelled by the input focusing matrix  $\mathbf{H}_{\text{in}} = [H_{\text{in}}(\mathbf{r}, \mathbf{r}_{\text{in}})]$  whose columns correspond to each input focal spot in the sample plane for each incident focusing point  $\mathbf{r}_{\text{in}}$ . (C) The return trip of the wave from the sample to the CCD camera is modeled by the transmission matrix  $\mathbf{G} = [G(\mathbf{u}_{\text{out}}, \mathbf{r})]$  that connects each point  $\mathbf{r}$  in the focal plane to each pixel  $\mathbf{u}_{\text{out}}$  of the CCD camera. (D) Finally, based on these propagation matrices and the sample reflectivity matrix  $\mathbf{\Gamma}$ , the reflection matrix  $\mathbf{R}$  can be simply expressed as the matrix product of these three matrices [Eq.1].